Rev. Roum. Sci. Techn.– Électrotechn. et Énerg.
Vol. **71**, *4*, pp. 549–554, Bucarest, 2026

ADVANCED CONTROL OF GRID-CONNECTED PHOTOVOLTAIC-FUEL CELL-BATTERY VIA SHUNT ACTIVE POWER FILTERS

FATIMA ZAHRA AMATOUL[1], HOMÈRE NKWAWO[2]

Keywords: Photovoltaic (PV); Maximum power point tracking (MPPT); Perturb and observe (P&O); Fuel cell; Battery; Boost converter; Buck converter; Dynamic modeling; DC-DC regulator; Inverter; Shunt active power filters (SAPF); Phase-locked loop (PLL).

Decentralized energy sources with highly variable outputs can cause power disturbances due to impedance asymmetries, short-circuiting, and load imbalances. The effectiveness of harmonic compensation depends on the chosen identification method; among these, three main detection strategies are used. This paper proposes a voltage-imbalance compensation method for the studied system based on active filtering with dq0-coordinate regulation. This widely used closed-loop approach ensures high steady-state accuracy and fast dynamic response.

1. INTRODUCTION

The quality of electrical energy is linked to the level of user satisfaction and becomes an important concern for energy distributors and their customers. Several studies have been carried out to reduce the harmful effects linked to harmonics [1,2]. The objective of the system studied in this work is to supply photovoltaic energy to both three-phase and single-phase loads, at a sinusoidal voltage with constant amplitude and frequency. An unbalanced three-phase electrical load can cause voltage imbalances between phases. To resolve this problem, a solution for depolluting electrical networks has been proposed, and it consists of active filters that are more flexible and less bulky, based essentially on voltage inverters controlled either by hysteresis or by pulse width modulation (PWM) [3]. Their principle, mathematically speaking, is the production and injection of harmonic currents or voltages of equal amplitude and in phase opposition with the harmonics produced by the non-linear load and which we wish to compensate, which makes it possible to keep the sinusoidal network current at any time. Physically, the SAPF operates as a controlled current source, injecting harmonic and reactive components to cancel load distortions [20,22]. It draws minimal active power from the grid only to maintain the DC-link voltage and compensate for internal losses.

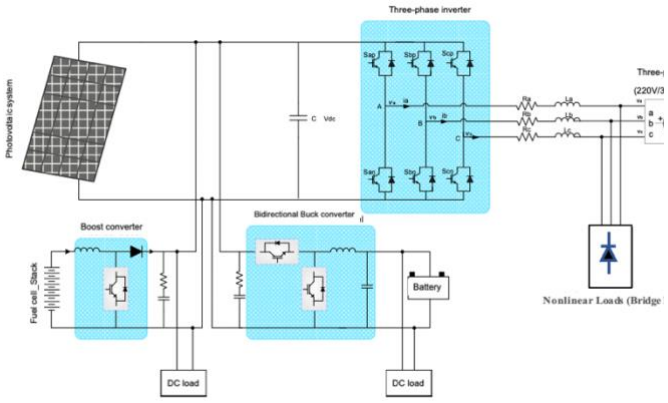


Fig. 1 – Architecture of the decentralized energy system connected to the network electrical distribution.

2. CONFIGURATIONS

2.1 PV SYSTEM TO GRID INTERFACE

Maximum power point tracking (MPPT) is commonly implemented via perturb and observe (P&O) or incremental conductance (INC) methods [9], with P&O favored for its Simplicity despite drawbacks such as slow response, steady-state oscillations, and reduced accuracy under rapidly varying conditions [4,5].

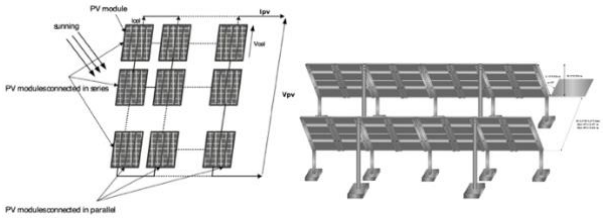


Fig. 2 – Photovoltaic installation example.

The DC/DC boost converter maximizes power transfer from the PV module to the load by adjusting its duty cycle to match the source impedance at the MPP, with the PV voltage reference serving as a tension setpoint if filtering is omitted [6]. By omitting the DC-DC boost converter, the system is simplified, with the DC-bus voltage directly regulated by the primary source control.

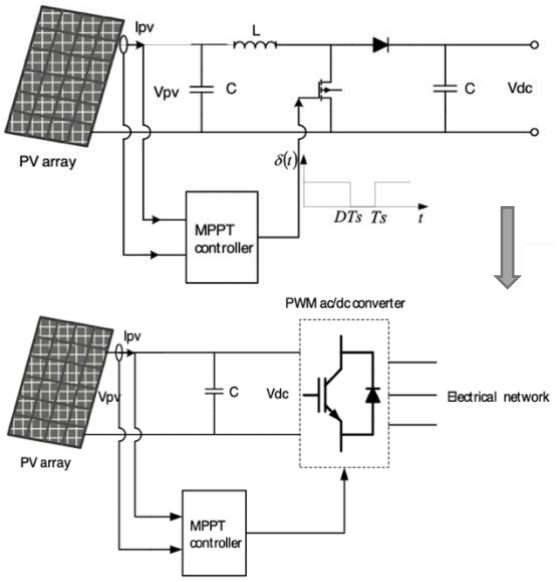


Fig. 3 – Simplified structure.

Simulink is used to develop the model of a solar PV array. The equations of a common model of a solar cell [7], as depicted in Fig. 4, are utilized for the PV array. The solar cell's voltage and current are as follows:

$$I_{cell} = I_{ph} - I_D - \left(\frac{V_{cell} + R_s I_{cell}}{R_P}\right), \quad (1)$$

[1]High School of Technology Essaouira, Cadi Ayyad University, Km9 Agadir Road, Essaouira Aljadida, Essaouira 44000, Morocco.
[2]Institute of Technology (IUT)-Villetaneuse, Sorbonne Paris Nord University, France.
Emails: fz.amatoul@uca.ma, homere.nkwawo@univ-paris13.fr

DOI: 10.59277/RRST-EE.2026.4.12

$$I_D = I_{sat}\left\{\exp\left[\frac{q}{KT}(V_{cell} + R_s I_{cell})\right] - 1\right\}, \quad (2)$$

where the output voltage and current of the cell are indicated by V_{cell} and I_{cell}.

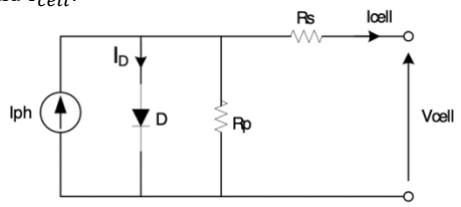


Fig. 4 – Photovoltaic cell equivalent model

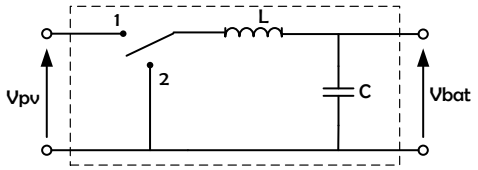


Fig. 5 – Circuit diagram of buck converter.

System efficiency is enhanced by using a DC-DC converter to match supply and load voltages, while maintaining a constant output voltage under variable input or load conditions via converter control. The inductor and capacitor waveforms form the basis of the modeling procedure (Fig. 5).

Parameters of the solar PV module from the datasheet are specified in Table 1.

Table 1

Key specifications of the PV module.

Parameters	Value
Temperature (T)	25 °C
Maximum power (P_{max})	90 W_p
Open-circuit voltage (V_{oc})	65.2 V
Short-circuit current (I_{sc})	2.11 A
Voltage, max power (V_{mpp})	49.3 V
Current, max power (I_{mpp})	1.83 A

2.2 BATTERY SYSTEM TO GRID INTERFACE

The battery model is based on a lead-acid PSpice representation [8], with PbO_2 anode and Pb cathode in sulfuric acid, operating in charging or discharging modes depending on the current direction.

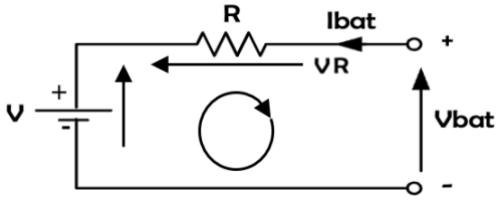


Fig. 6 – Battery model [6].

The battery's terminal voltage during the charging mode (where the current flows into the positive terminal, *i.e.*, $I_{bat} > 0$) can be formulated using Kirchhoff's voltage law based on the reference loop shown in Fig. 6,

$$V_{bat} = V - RI_{bat}, \quad (3)$$

where V is the open-circuit voltage, R is the internal resistance, $V_R = RI_{bat}$ is the voltage drop across the internal resistance, and I_{bat} is the battery current (taken as positive during charging and negative during discharging). Depending on the operational mode the battery is in, a separate set of equations determines V and R.

2.3 DC-DC REGULATOR SYSTEM

The battery has a nominal voltage of 48 V. A PID controller is used to regulate the DC-DC converter, ensuring a stable output regardless of the battery's terminal voltage fluctuations (typically between 42 V and 54 V), ensuring voltage regulation under load or PV variations, while a dynamic model incorporating inductor and capacitor behavior provides the basis for system design and stability analysis (Fig. 7) [9].

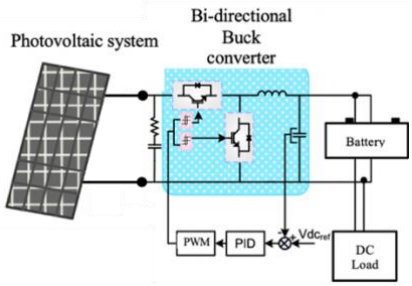


Fig. 7 – The converter power stage and a feedback network.

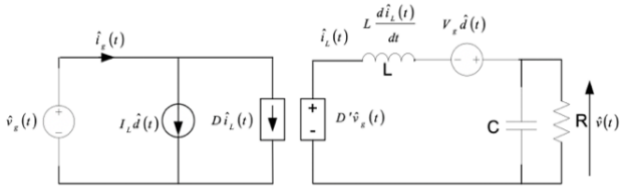


Fig. 8 – DC-DC regulator system with a small-signal converter's buck equivalent circuit.

The PID control system should have a high gain at low frequencies and a steep gain curve at the crossover frequency to ensure stability, and it must also ensure sufficient phase margin. A closed-loop PID-driven buck converter, well-sized, performs better in both transient and steady-state conditions [10].

2.4 FUEL CELLS TO GRID INTERFACE

A fuel cell converts the chemical energy of a fuel into electricity and, unlike batteries, operates continuously with renewed reactants. Six main fuel cell technologies exist, distinguished by their electrolyte and operating temperature [11]. The proton exchange membrane fuel cell (PEMFC), noted for its low-temperature operation, fast startup, and high-power density, is widely used in transport, stationary, and portable applications. Our study, therefore, focuses on a PEMFC system [12].

2.4.1 OPERATING CONCEPT OF PEMFC (PROTON EXCHANGE MEMBRANE FUEL CELL)

A chemical reaction describes the fuel cell's working principle. This chemical reaction is an electrochemical oxidation-reduction process. According to the overall chemical reaction, hydrogen and oxygen combine to generate heat, water, and electricity

$$2\,H^+ + O_2 \rightarrow 2H_2O + \text{electricity} + \text{heat}. \quad (4)$$

At the anode, hydrogen is oxidized to two protons H^+ and two electrons e^-, while at the cathode, it is reduced to water by interaction with two protons H^+ and two electrons e^-. Therefore, the two half-processes of oxidation and reduction are as follows:

$$\text{Anode} \quad H_2 \rightarrow 2\,H^+ + 2e^-, \quad (5)$$

$$\text{Cathode} \quad 2H^+ + 2e^- + \frac{1}{2}\,O_2 \rightarrow H_2O. \quad (6)$$

2.4.2 MODELING OF THE FUEL CELL SYSTEM

Equation (7) defines the expression of the voltage created in the absence of electric current [13]. We obtain a static characteristic in the presence of an electric current, and Fig. 9 shows its general form [14].

$$E_{(P,T)} = 1.23 - 0{,}85.10^{-3}(T - 298.15) + \\ +4.3085 \cdot 10^{-5} T\left(\ln P_{H_2} + 0.5 \cdot \ln P_{O_2}\right). \quad (7)$$

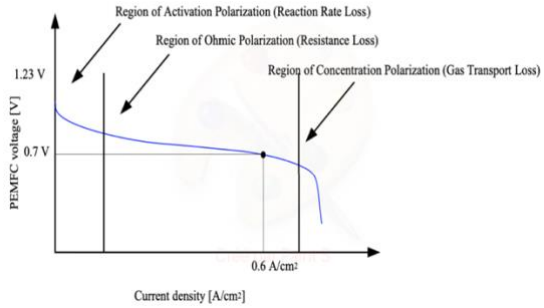


Fig. 9 – Polarization curve.

Here is how the actual fuel cell voltage will be determined: experimental tests validate the empirical equations that underpin the PEMFC model. A single-cell PEMFC voltage at the output is explained as follows [16]:

$$V_{Fuel_cell} = \\ \left(\begin{array}{c} 1.23 - 0.85.10^{-3}(T - 298.15) + \\ 4.3085 \cdot 10^{-5} \cdot T \cdot \left(\ln P_{H_2} + 0.5 \cdot \ln P_{O_2}\right) - \\ \frac{I}{A}\left(\frac{181.6 \cdot \left[1 + 0.03\left(\frac{I}{A}\right) + 0.062 \cdot \left(\frac{T}{303}\right)^2 \cdot \left(\frac{I}{A}\right)^{2.5}\right]}{\left[\lambda_{\left(\frac{H_2O}{SO_3^-}\right)} - 0.634 - 3 \cdot \left(\frac{I}{A}\right)\right] \cdot \exp\left[4.18 \cdot \left(\frac{T - 303}{T}\right)\right]} \cdot l + A \cdot R_C \right) \\ -B \cdot \ln\left(1 - \frac{I + I_n}{I_L}\right). \end{array} \right) \quad (8)$$

This last equation depicts the fuel cell's static electrochemical activity, where T [K] is the operating temperature, P_{H2}, P_{O2} [atm] are respectively the partial pressures of hydrogen and oxygen, I [A] is the operating current of the cell and A [cm^2] is the active surface area of the cell, λ is the water content in the membrane (ranging from 0 to 22), l [µm] represents the membrane thickness, R_C [Ω] is the equivalent contact resistance to electron conduction, B is the coefficient of the transport term, I_n [A] is the internal leakage current, and I_L [A] is the limiting current.

2.5 DC-DC REGULATOR SYSTEM

Given the high-voltage dynamics of a fuel cell, a power converter connected to it produces a steady voltage. Among the preferred topologies for use in fuel cell systems is the boost converter; it can apply a high degree of filtering to the input current. This allows for optimal control of the cell voltage, and the converter is composed of only one controlled switch [15].

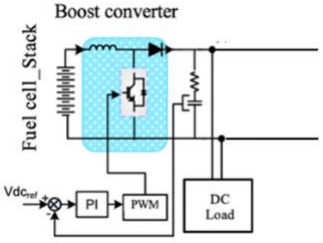


Fig. 10 –Typical structure of fuel cell-boost converter.

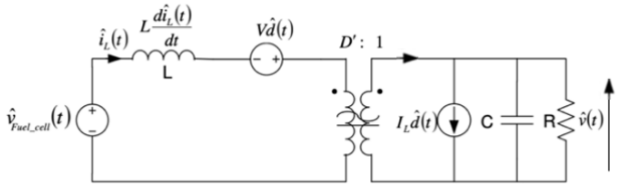


Fig. 11 –Small-signal equivalent circuit.

The converter is modeled using the small-signal averaged approach [16], capturing system nonlinearities around an operating point. Control objectives are set through the reference signals i_{Lref} and v_{ref}. For low-power converters, the current loop can be omitted, and the PWM modulator is driven directly by the voltage controller (Fig. 12). The open-loop converter. The study reported in [17] provides Laplace-transform transfer functions obtained from the average small-signal model (Fig. 11).



Fig. 12 – Closed-loop control system configuration.

The PEM fuel cell (PEMFC) stack is dimensioned for a maximum power of 5 kW. To ensure a DC-DC converter duty cycle of 0.5, the stack voltage is set at 280 V, requiring 528 cells in series. The nominal parameters are summarized in Table 2.

Table 2

PEM fuel cell rated parameters

Parameters	Value
PEMFC Nominal Power (P_{FC})	5 kW
Number of cells (N_{cell})	528
Single cell voltage (E_{cell})	0.53 V
Stack Voltage (V_{Fuel_cell})	280 V

3. PRINCIPLES OF ACTIVE FILTERING

The parallel active filter (Fig. 13) operates as a current source, injecting currents opposite to those of the polluting load, so the network current remains sinusoidal. Its purpose is to block unbalanced, reactive, and harmonic currents from propagating upstream [18,19].

3.1 DQ0 COMMAND STRATEGY

The dq0 control strategy (Fig. 13) employs nested voltage and current loops, with a PLL extracting the fundamental positive-sequence network voltage to serve as a precise reference for identification and control [20,21].

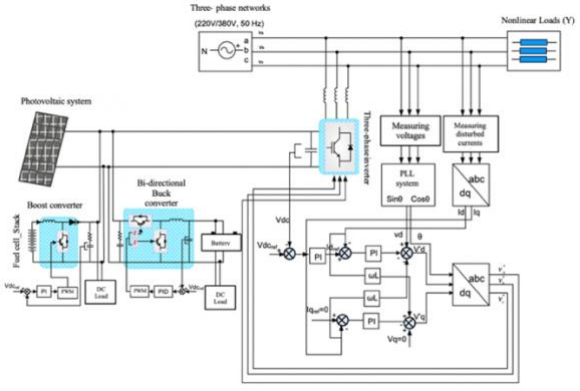


Fig. 13 – dq0 command strategies.

To obtain the model of the converter and its supply in the synchronous rotating (d,q) reference frame, the $\alpha\beta - dq$ transformation is applied:

$$[P(\theta)][i(t)]_{\alpha\beta} = [i(t)]_{dq}, \quad (9)$$

$$\frac{\mathrm{d}[i(t)]_{\alpha\beta}}{\mathrm{d}t} = \frac{\mathrm{d}[P(\theta)]^{-1}}{\mathrm{d}t}[i(t)]_{dq} + [P(\theta)]^{-1}\frac{\mathrm{d}[i(t)]_{dq}}{\mathrm{d}t}, \quad (10)$$

with

$$P(\theta) = \begin{bmatrix}\cos\theta & -\sin\theta \\ \sin\theta & \cos\theta\end{bmatrix}. \quad (11)$$

Then

$$P(\theta)\frac{\mathrm{d}[P(\theta)]^{-1}}{\mathrm{d}t} = \omega\begin{bmatrix}\cos\theta & -\sin\theta \\ \sin\theta & \cos\theta\end{bmatrix}\begin{bmatrix}-\sin\theta & \cos\theta \\ -\cos\theta & -\sin\theta\end{bmatrix} = \omega\begin{bmatrix}0 & 1 \\ -1 & 0\end{bmatrix}, \quad (12)$$

where $\theta = \omega t$ represents the angular position of the rotating reference frame.

Finally, the characteristic equations in the dq0 frame are:

$$\begin{bmatrix}V_d'(t) \\ V_q'(t)\end{bmatrix} = \quad (14)$$

$$\begin{bmatrix}v_d(t) \\ v_q(t)\end{bmatrix} - R\begin{bmatrix}i_d(t) \\ i_q(t)\end{bmatrix} - \omega L\begin{bmatrix}0 & 1 \\ -1 & 0\end{bmatrix}\begin{bmatrix}i_d(t) \\ i_q(t)\end{bmatrix} - L\frac{\mathrm{d}}{\mathrm{d}t}\begin{bmatrix}i_d(t) \\ i_q(t)\end{bmatrix}, \quad (15)$$

Thus, the control signals are

$$V_d'(t) = v_d(t) - Ri_d(t) - \omega Li_q(t) - L\frac{\mathrm{d}i_d(t)}{\mathrm{d}t}, \quad (16)$$

$$V_q'(t) = v_q(t) - Ri_q(t) + \omega Li_d(t) - L\frac{\mathrm{d}i_q(t)}{\mathrm{d}t}. \quad (17)$$

3.2 DC VOLTAGE REGULATION

The storage capacitor mitigates power fluctuations from reactive currents, harmonics, and converter losses, while maintaining a constant average voltage.

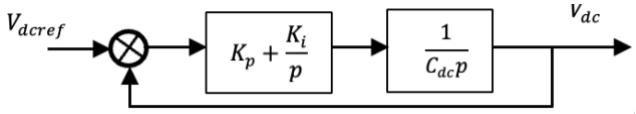


Fig. 14 – DC-side voltage regulation with a PI.

Following a difference between V_{dcref} and V_{dc}, the current at the regulator output is added to the fluctuating active current and gives rise to an active fundamental current, thus correcting the voltage. To carry out this regulation, we can choose between a proportional regulator and an integral-proportional regulator. The latter is often preferable because it allows the static error to be canceled [22].

The reference currents i_{dref} and i_{qref} are the outputs of the PI used in the external voltage regulation loop v_d and v_q. This regulation loop makes it possible to set the amplitude of the DC voltage.

$$i_{dref} = (PI)\left(v_{dref} - v_d\right), \quad (18)$$

$$i_{qref} = (PI)\left(v_{qref} - v_q\right), \quad (19)$$

The closed-loop transfer function

$$\frac{v_{dc}}{v_{dcref}} = \frac{\frac{K_i}{C_{dc}} + \frac{K_p}{C_{dc}}p}{p^2 + \frac{K_p}{C_{dc}}p + \frac{K_i}{C_{dc}}} \quad (20)$$

where p denotes the Laplace operator.

By identifying the closed-loop transfer function from the system to a second-order system, we obtain the equality,

$$\frac{1 + T_i p}{1 + T_i p + \frac{T_i C_{dc}}{K_p}p^2} = \frac{1 + T_n p}{1 + \frac{2\xi}{\omega_n}p + \frac{1}{\omega_n^2}p^2}, \quad (21)$$

with

$$\omega_n^2 = \frac{K_i}{C_{dc}}, \xi = K_p\sqrt{\frac{1}{C_{dc}K_i}} \text{ and } \frac{K_p}{K_i}. \quad (22)$$

where C_{dc} represents the DC-link capacitance, K_p and K_i are the proportional and integral gains of the DC-voltage PI controller, T_i is the integral time constant, ω_n is the natural angular frequency, and ξ denotes the closed-loop damping ratio.

3.3 AC SIDE CURRENT REGULATION

AC current regulation aims for a sinusoidal current with unity power factor and controllable DC-link voltage [23], achieved by setting d- and q-axis current references: q-axis reference at zero for unity power factor and d-axis controlled via a PI regulator based on the DC voltage error [24]. According to the equations, and by doing the Laplace transform, the equations modeling our system can be written as follows [25]:

$$Lpi_d(p) = -Ri_d(t) - \omega Li_q(p) + v_d(p) - V_d'(p), \quad (23)$$

$$Lpi_q(p) = -Ri_q(t) + \omega Li_d(p) + v_q(p) - V_q'(p), \quad (24)$$

We define two terms $u_d(t)$ and $u_q(t)$ such that

$$u_d(p) = -\omega Li_q(p) + v_d(p) - V_d'(p), \quad (25)$$

$$u_q(p) = +\omega Li_d(p) + v_q(p) - V_q'(p), \quad (26)$$

with

$$\begin{cases}u_d(p) = (Lp + R)i_d(p), \\ u_q(p) = (Lp + R)i_q(p).\end{cases} \quad (27)$$

Two PI regulators are used to control the current components of the inverter. For our regulator, we use a PI regulator with pole compensation, shown in Fig. 15.

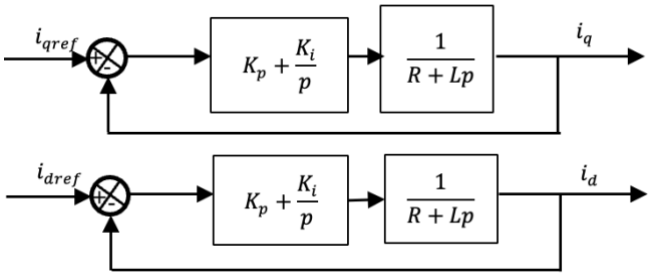


Fig. 15 – Regulation of input currents with a PI as a rotating reference.

It is the regulator most classically used for controlling continuous and sampled systems. It consists of two terms: a proportional and an integral term.

Such a controller has the transfer function

$$C_{PI}(p) = K_p\left(\frac{1 + T_i p}{T_i p}\right). \quad (28)$$

The open-loop transfer function of the PI regulator associated with the transfer function on the DC side is

$$G_{BO}(p) = K_p\left(\frac{1 + T_i p}{T_i p}\right)\left(\frac{1}{R + Lp}\right). \quad (29)$$

The PI regulator is designed with a time constant equal to L/R; the closed-loop transfer function is $G_{BF}(p) = 1/\left(1 + \left(L/K_p\right)p\right) = 1/(1 + \tau p)$ with $t = L/K_p$ and $K_i = R/L$.

4. OPTIMIZATION RESULTS AND DISCUSSION

The simulation results for the proposed hybrid system are illustrated in Figs. 16 to 24. They confirm the high performance of the proposed control strategy. As shown in Fig. 18, the DC-link voltage V_{DC} remains perfectly regulated at its reference value, proving the robustness of the external voltage loop despite power fluctuations.

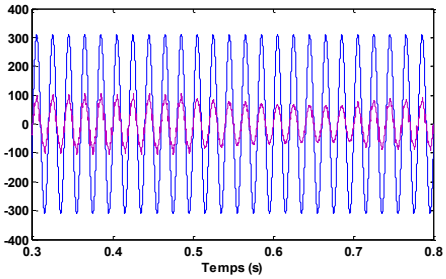


Fig. 16 – Source voltage and current.

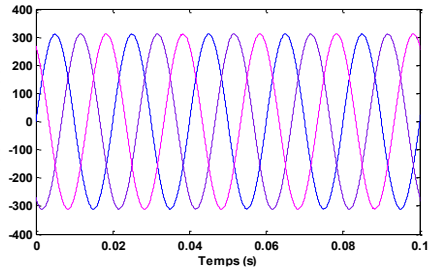


Fig. 17 – Source voltages.

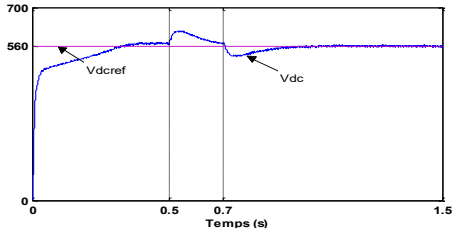


Fig. 18 – DC side voltage V_{dc}.

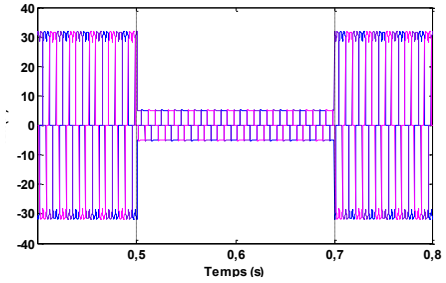


Fig. 19 – Nonlinear load currents.

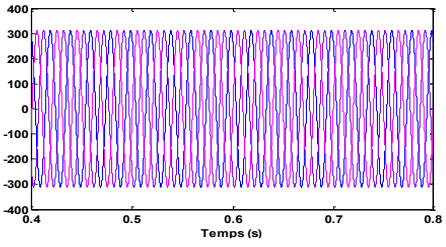


Fig. 20 – Nonlinear load voltages.

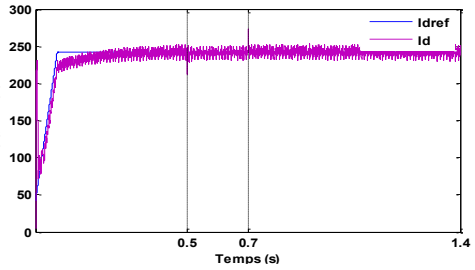


Fig. 21 – The direct current I_d in the dq0 frame of reference.

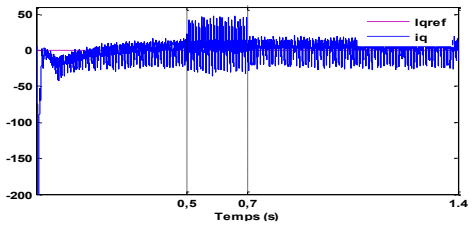


Fig. 22 – The direct current I_q in the dq0 frame of reference.

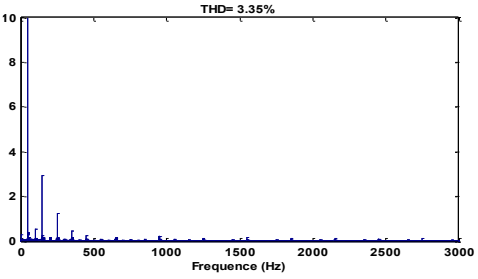


Fig. 23 – Spectral analysis of source current.

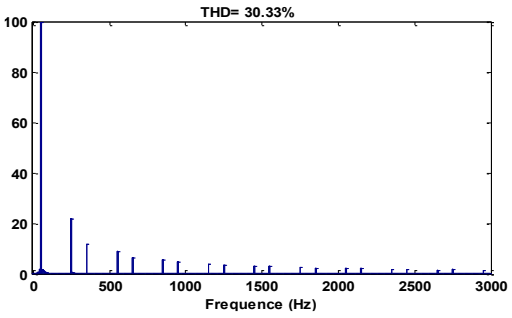


Fig. 24 – Spectral analysis of load current.

Furthermore, the internal regulation loop ensures that the d- and q-current components strictly follow their references. Consequently, the grid currents (shown in Fig. 23) are sinusoidal with a THD of 3.35%, which is well within the IEEE-519 standard limits, and remain in phase with the voltages. This validates effective harmonic compensation by the SAPF and a seamless power balance among the PV array, the Fuel Cell, and the Battery.

5. CONCLUSION

This study successfully integrated a hybrid PV-FC-Battery system with a Shunt Active Power Filter to address energy management and power quality challenges. The developed control strategy demonstrates high reliability in maintaining a stable DC bus and ensuring a clean grid current injection, as evidenced by the low harmonic distortion obtained. By accurately sizing the 5-kW PEMFC and the storage unit, the system achieves a balanced power flow even

under fluctuating environmental conditions. This approach provides a robust framework for improving the efficiency and stability of decentralized microgrids, laying the groundwork for future optimizations in smart grid applications.

CREDIT AUTHORSHIP CONTRIBUTION

Fatima Zahra AMATOUL and Homère NKWAWO both designed the study, performed the analysis, developed the software, and drafted the manuscript. All authors reviewed and approved the final version.

Received on 1 December 2025

REFERENCES

1. M.W. Qaisar, J. Lai, J. Fang, "Modeling and control of grid-forming active power filters for harmonic suppression and enhanced power quality," Applied Sciences, **15**, pp. 1–10 (2025).
2. L. Saihi, B. Berbaoui, "Advanced control for photovoltaic-unified power quality conditioner systems: a simulation approach," Rev. Roum. Sci. Techn. – Électrotechn. Et Énerg., **70**, *4*, pp. 537–542 (2025).
3. Z. Lammouchi, C. Labiod, K. Srairi, M. Benbouzid, "Enhanced model-free predictive control for voltage source inverters using an adaptive observer," Rev. Roum. Sci. Techn. – Électrotechn. Et Énerg., **69**, *3*, pp. 317–322 (2024).
4. N. Karami, N. Moubayed, R. Outbib, "General review and classification of different MPPT techniques," Renewable and Sustainable Energy Reviews, **68**, pp. 1–18 (2017).
5. A. Mohapatra, B. Nayak, P. Das, K.B. Mohanty, "A review on MPPT techniques of PV system under partial shading condition," Renewable and Sustainable Energy Reviews, **80**, *4*, pp. 854–867 (2017).
6. L. Zaghba, A. Borni, M.K. Benbitour, A. Fezzani, H. Alharbi, E. Ali, A.M. Amsal, S.S.M. Ghoneim, "Design and implementation of a predictive current control strategy for enhanced performance of DC–DC boost converter applications," Results in Engineering, **28**, pp. 1–10 (2025).
7. F.Z. Amatoul, M.T. Lamchich, A. Outzourhit, "Design control of DC/AC converter for a grid-connected PV systems using Matlab/Simulink," I. RE.MO.S, **5**, pp. 128–136 (2012).
8. A. Rahmoun, H. Biechl, A. Rosin, "Evaluation of Equivalent Circuit Diagrams and Transfer Functions for Modeling of Lithium-Ion Batteries," Electrical, Control and Communication Engineering, **2**, (2013).
9. S. Subiyanto, A. Mohamed, M.A. Hannan, "Development of an efficient photovoltaic maximum power point tracking controller," IEEE International Electric Machines & Drives Conference (IEMDC), pp. 1189-1194 (2011).
10. R.W. Erickson, D. Maksimovic, "Fundamentals of Power Electronics," 2nd ed., Kluwer Academic Publishers, pp. 394–401 (2001).
11. A. Baroutaji, T. Wilberforce, M. Ramadan, A.G. Olabi, "Comprehensive investigation on hydrogen and fuel cell technology in the aviation and aerospace sectors," Renewable and Sustainable Energy Reviews, **106**, pp. 31–40 (2019).
12. A. Vasilyev, J. Andrews, L.M. Jackson, S.J. Dunnett, B. Davies, "Component-based modeling of PEM fuel cells with bond graphs," International Journal of Hydrogen Energy, **42**, *49*, pp. 29406–29421 (2017).
13. K. Steffen, R. Hanke-Rauschenbach, "Fuel Cell Systems: Modelling, Control and Applications," Springer, pp. 1–300 (2021).
14. O. Kuznyetsov, I. Bilyakovskyy, "Modeling of a PEM fuel cell polarization curve by low-order polynomials for the output power calculation algorithms," Rev. Roum. Sci. Techn. – Électrotechn. Et Énerg., **69**, *2*, pp. 249–254 (2024).
15. J.G. Kassakian, M.F. Schlecht, G.C. Verghese, "Principles of Power Electronics," Addison-Wesley, pp. 1–400 (1991).
16. H. Abu-Rub, M. Malinowski, K. Al-Haddad, "Power Electronics for Renewable Energy Systems, Transportation and Industrial Applications," IEEE Press–Wiley, pp. 1–856 (2014).
17. D.W. Spier, G. Oggier, S.A. Oliveira da Silva, "Modeling and analysis of a DC–DC boost–buck converter for renewable energy applications," 14th Brazilian Power Electronics Conference, pp. 1–9 (2017).
18. B.W. França, M. Aredes, L. Francisco da Silva, G.F. Gontijo, T.C. Tricarico, J. Posada, "An enhanced shunt active filter based on synchronverter concept," IEEE Journal of Emerging and Selected Topics in Power Electronics, **10**, pp. 494–505 (2021).
19. S.F. Al-Gahtani, Z.M.S. Elbarbary, S.M. Irshad, "A developed DQ control method for shunt active power filter to improve power quality in transformers," PLOS ONE Journal, **19**, *7*, pp. 1–18 (2024).
20. P. Tripathy, B. Misra, B. Nayak, "Phase-locked loop-based synchronization schemes for three-phase unbalanced and distorted grid: a review," International Journal of Applied Power Engineering, **13**, *4*, pp. 934–943 (2024).
21. P. Chittora, A. Singh, M. Singh, "Adaptive EPLL for improving power quality in three-phase three-wire grid-connected photovoltaic system," IET Renewable Power Generation, **13**, *9*, pp. 1595–1602 (2019).
22. J. Pérez-Ramírez, D. Montoya-Acevedo, W. Gil-González, O.D. Montoya, C. Restrepo, "Shunt active power filter using model predictive control with stability guarantee," ePrime – Advances in Electrical Engineering, Electronics and Energy, **12**, pp. 1–11 (2025).
23. Q. Yuan, "Current loop high-performance compensation control strategy analysis of active power filter," Physics Procedia, **24**, pp. 883–890 (2012).
24. N.L. Surasmi, G. Shiny, B.R. Vinod, "Enhancing grid power quality with shunt active filter and unified power quality conditioner," Journal of Electrical Systems, **20**, *3*, pp. 7755–7773 (2024).
25. L. Xia, W. Cong, C. Hong, C. Hua, K. Jiayi, "Research on characteristic and DC voltage balancing control of a novel three-phase line-voltage cascaded unity power factor rectifier under unbalanced grid," IET Power Electronics, **17**, pp. 2971–2985 (2024).